Multiple-humped fission and fusion barriers of the heaviest elements and ellipsoidal deformations

Guy Royer, Christelle Gautier

Multiple-humped fission and fusion barriers of the heaviest elements and ellipsoidal deformations

G. Royer* and C. Gautier
Laboratoire Subatech,
UMR : IN2P3/CNRS-Université-Ecole des Mines,
44307 Nantes Cedex 03, France

The deformation energy in the fusionlike deformation path has been determined from a generalized liquid drop model taking into account both the proximity energy, the asymmetry and the microscopic corrections. Multiple-humped potential barriers appear in the exit and entrance channels of the heaviest elements. In the fission path of actinides, the second maximum corresponds to the transition from compact and creviced one-body shapes to two touching ellipsoids. A third peak appears in certain asymmetric exit channels where one fragment is almost a double magic nucleus with a quasi-spherical shape while the other one evolves from oblate to prolate shapes. The heights of the double and triple-humped fission barriers and the predicted half-lives of actinides follow the experimental results. In the fusion path leading possibly to superheavy elements, double-humped potential barriers appear for cold fusion but not for warm fusion. The α decay half-lives can be reproduced using the experimental Q_α value.

I. INTRODUCTION

Experimentally, the ground state and isomeric state spectra of actinides indicate the existence of double-humped potential barriers and the fission probability and the angular distribution of the fragments even suggest the presence of hyperdeformed states in a deep third well in several Th and U isotopes [1]. The heights of the inner and outer peaks are almost constant (5-6 MeV) from Th to Am isotopes [2] and the same values are even advanced for superheavy nuclei [3]. The many quasi-fission events observed in the reactions carried out to form superheavy elements are possibly due to the existence of an external large potential well in double-humped fusion barriers.

It has been shown within a Generalized Liquid Drop Model that the introduction of the proximity energy between opposite surfaces lowers the deformation energy in the quasi-molecular shape path and allows to reproduce the barrier heights of the fission [4], cluster emission and α decay [5, 6] processes in this exit channel as well as the highly deformed state data [7].

In the present study, to investigate the exit channels in the actinide region the ellipsoidal deformations of the fission fragments have been taken into account as the shell and pairing energies [8] while for the entrance channels of the superheavy elements the spherical shapes have been assumed and the experimental Q value has been introduced empirically.

II. POTENTIAL ENERGY AND QUASI-MOLECULAR SHAPES

In the GLDM, the potential energy is the sum of the volume, surface, Coulomb and proximity energies. The selected values for the volume and surface coefficients are a_v=15.494 MeV, a_s=17.9439 MeV, k_v=1.8 and k_s=2.6 and the radius is given by $R = 1.28A^{1/3} - 0.76 + 0.8A^{-1/3}$. Recently [9], different combinations of terms used to reproduce the nuclear binding energy have

*Electronic address: guy.royer@subatech.in2p3.fr

been compared (see Table 1) using the following expansion

$$B_{nucl} = a_v(1-k_vI^2)A - a_s(1-k_sI^2)A^{2/3} - \frac{3}{5}\frac{e^2Z^2}{R_0} \quad (1)$$
$$+E_{pair} - E_{shell} - a_kA^{1/3} - a_0A^0 - f_p\frac{Z^2}{A} - W|I|.$$

The values used in the GLDM are close to the ones given σ=0.60 MeV in the table.

TABLE I: Dependence of the energy coefficient values (in MeV) on the selected term set including or not the pairing and shell energies and the corresponding root mean square deviations. The Coulomb energy coefficient is not adjusted and is determined by $\frac{3}{5}\frac{e^2Z^2}{1.28A^{1/3}-0.76+0.8A^{-1/3}}$.

a_v	k_v	a_s	k_s	a_k	a_0	f_p	W	*Pairing*	*Shell*	σ
15.9622	1.7397	18.0108	1.0627	-	-	-	-	n	n	3.12
15.8809	1.7201	17.5366	0.8234	-	-	-	-	n	y	1.56
15.8846	1.7256	17.5547	0.8475	-	-	-	-	y	y	1.32
15.8533	1.8937	17.2793	1.9924	-	-	-	44.4714	y	y	1.04
15.5887	1.8011	18.194	1.7271	-	-	-1.98718	-	y	y	0.83
15.6089	1.9136	17.9021	2.4111	-	-	-1.69912	32.1647	y	y	0.599
15.5833	1.8988	17.726	2.3495	0.433	-	-1.73074	29.8599	y	y	0.598
15.5996	1.9061	17.8631	2.3757	-	0.3146	-1.71583	31.0077	y	y	0.599
15.3737	1.8892	14.9364	2.5745	12.418	-16.7906	-1.71391	27.8208	y	y	0.58

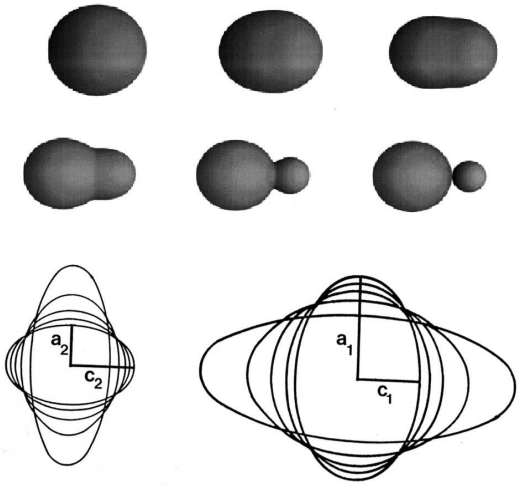

FIG. 1: Shape sequence describing the one-body shape evolution and two coaxial ellipsoid configurations.

The one-body shape sequence [4–8], allows to simulate the development of a deep neck in compact and little elongated shapes with almost spherical ends (see Fig. 1). For two-body shapes, the coaxial ellipsoidal deformations have been considered [10] for the exit channel of actinides. The proximity energy which takes into account the effects of the attractive nuclear forces between nucleons facing each other across the neck or the gap depends explicitly on the

selected shapes all along the deformation path. For these quasi-molecular shapes, the proximity energy is very important.

The shape-dependent shell corrections have been determined within the Droplet Model expressions [11] with slightly different values for the parameters [8]. For the study in the actinide region the selected highest proton magic number is 114 while, for the two highest neutron magic numbers, the values 126 and 184 have been retained. For the two-body shapes, the total shell energy is the sum of the shell corrections for each deformed fragment. The pairing energy has been calculated from the expressions proposed by the Thomas-Fermi model.

III. POTENTIAL BARRIERS

The dependence of the deformation energy on the selected shape sequence and introduction of the microscopic energies is displayed in Fig. 2 for an asymmetric fission channel of the ^{230}Th nucleus. The shell effects generate the deformed ground state and contribute to the formation

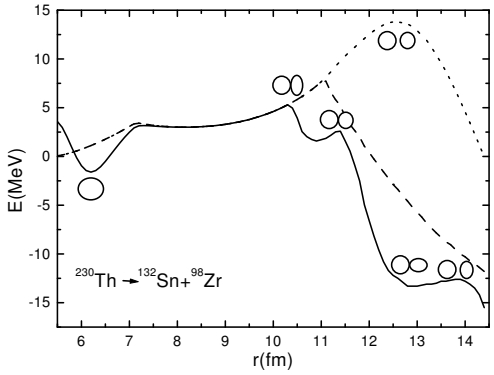

FIG. 2: Potential barrier for a ^{230}Th nucleus emitting a doubly magic nucleus ^{132}Sn. The dotted and dashed curves give the macroscopic energy for two-body shapes respectively within two spheres and ellipsoidal deformations. The solid line includes the shell and pairing corrections. r is the distance between mass centres.

of the first peak. The proximity energy flattens the potential energy curve and explains with the shell effects the formation of a deep second minimum lodging the isomeric states of heavier nuclei. In the exit channel via two-sphere approximation the top of the barrier is reached after the rupture of the matter bridge between the two spherical fragments ($r = 11.4$ fm). Then, the top corresponds to two separated fragments maintained in unstable equilibrium by the balance between the attractive nuclear forces and the repulsive Coulomb ones. In this mass range, the introduction of the microscopic corrections for two-sphere shapes does not allow to reproduce the experimental data on the fission barrier heights of actinide nuclei. When the ellipsoidal deformations of the fragments are taken into account, the transition corresponds to the passage (at $r = 11$ fm for ^{230}Th) from a one-body shape with spherical ends and a deep neck to two touching ellipsoidal fragments, one or both of them being slightly oblate. The barrier height is reduced by several MeV. The introduction of the shell effects still lowers the second peak and

shifts it to an inner position ($r = 10.3$ fm here). It even leads to a third minimum and third peak in this asymmetric decay path. A plateau appears also at larger distances around 10 MeV below the ground state. It is due to the persistence of the prolate deformation of the lightest fragment. The end of the plateau corresponds to the end of the contact between the two fragments and to a rapid transition from prolate to oblate shapes for the non-magical fragment and the vanishing of the proximity energy. Later on, this second fragment returns to a prolate shape when the interaction Coulomb energy vanishes. For the ^{238}U, ^{243}Pu and ^{250}Bk nuclei, selected

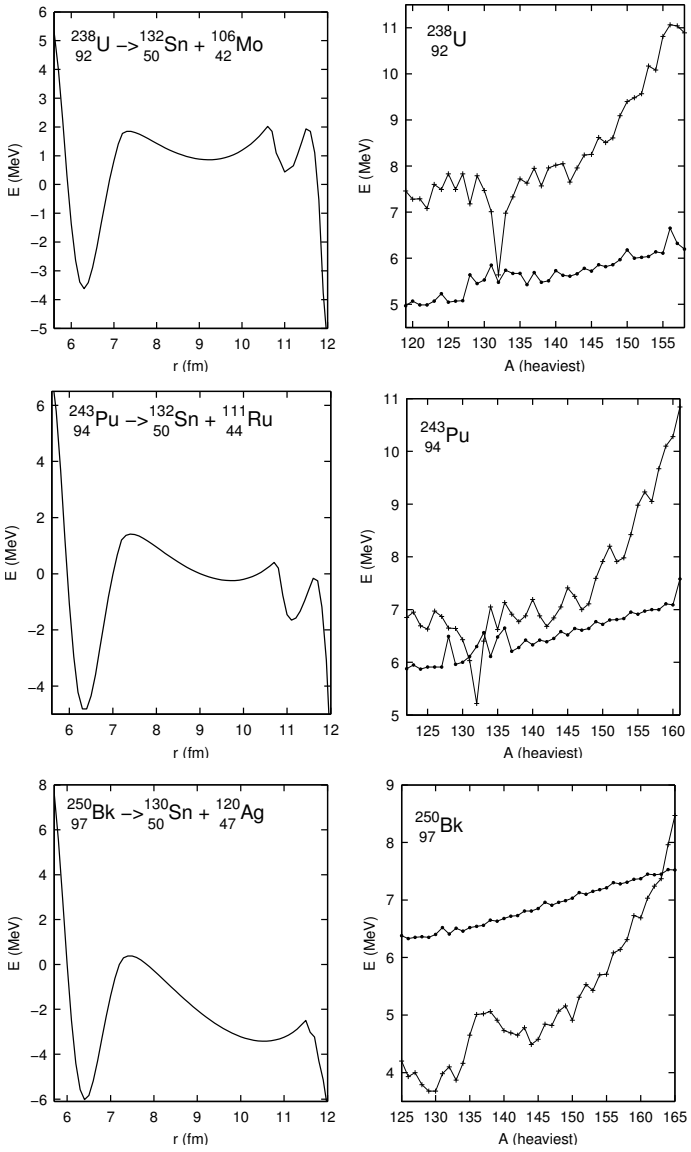

FIG. 3: On the left, multiple-humped potential barriers in the mentioned asymmetric fission path for ^{238}U, ^{243}Pu and ^{250}Bk. On the right, inner (full circles) and outer (crosses) fission barrier heights as a function of the heaviest fragment mass.

potential barriers are shown in Fig. 3. For a given mass asymmetry, the charge asymmetry which

minimizes the deformation energy has been retained. The proximity energy and the attenuated microscopic effects are at the origin of the second one-body shape minimum. The heights of the two peaks generally increase with the asymmetry but the shell and pairing corrections induce strong variations from this global behaviour. Their main effect is to favour, for the U and Pu isotopes, an asymmetric path where one fragment is close to the doubly magic $^{132}_{50}$Sn nucleus, and keeps a spherical shape. This effect is less pronounced for ^{250}Bk since for nuclei with $Z \sim 100$ the symmetric fission gives fragments with a charge of around 50. A third minimum and third peak exist only in the asymmetric decay path and for some specific isotopes. The calculated and experimental energies (in MeV) of the extrema of the potential barriers have been compared [8] and a good agreement exists for the two first peak heights. The still sparse but exciting data for the third barrier are also correctly reproduced.

IV. THIRD POTENTIAL BARRIER

The origin of the third well appearing in some exit channels is examined now. In the Fig. 4 the external part of the potential barriers in the symmetric case and an asymmetric one are compared in the lower part of the figure for ^{236}U. The dashed line represents the potential for two touching ellipsoids when the one-body shape is still energetically favoured.

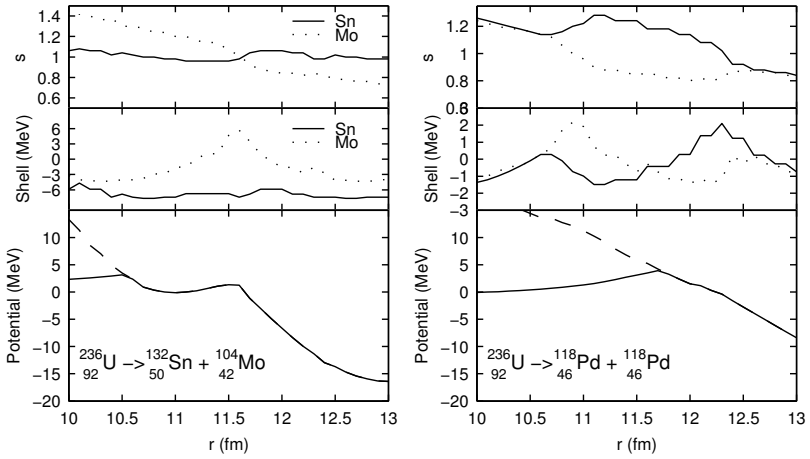

FIG. 4: Fission barriers, shell energies and ratio of the semi-axes of the two ellipsoidal fragments for an asymmetric decay channel and the symmetric one for ^{236}U. On the lowest part, the fission barrier is given by the solid line.

The second peak (but first on the figure) corresponds to the point where these touching ellipsoids lead to the lowest energy. The heaviest fragment is a magic nucleus which almost preserves its spherical shape. The non magic fragment was born in an oblate shape ($s \sim 1.4$), due to the small distance between the mass centres at this step. When this distance increases, the ratio s decreases, because of the proximity energy which tends to keep close the two tips of the fragments. Thus, the lightest fragment remaining in contact with the other spherical fragment approaches the spherical shape and its shell energy increases to reach a maximum which is at the origin of the third peak and which corresponds to two touching different spheres. Before reaching this third peak a third minimum appears. Its shape is hyperdeformed and asymmetric in agreement with the experimental data [1]. Later on, the proximity forces maintain the two fragments in contact and the shape of the smallest one evolves to prolate shapes ($s < 1$) and the

shell corrections decrease. The third barrier appears only in the asymmetric decay path of some specific nuclei. In the symmetric mass path, the proximity and Coulomb energies counterbalance the smallest shell effects and induce an asymmetric shape, the two fragments remain in contact but one fragment is oblate while the other one is prolate. With increasing distance between the mass centres the two nuclei become prolate.

The dependence of the fission barrier heights and profiles on the asymmetry are given in Fig. 5 for the ^{234}U nucleus, for which experimental data on the third barrier exist [1]. The position of the second peak in the symmetric decay path corresponds to the position of the third peak in the asymmetric deformation path. Clearly the magicity of some Sn isotopes plays the main role.

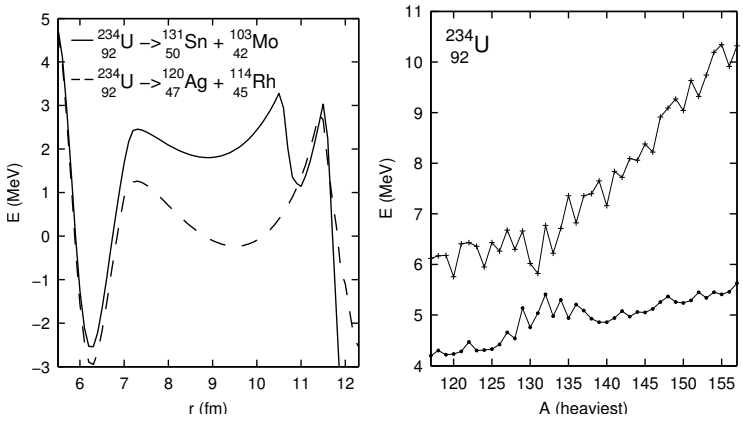

FIG. 5: Fission barriers for ^{234}U and two decay channels. The inner and outer fission barrier heights as functions of the asymmetry are given, on the right, respectively by the full circles and crosses.

V. ACTINIDE HALF-LIVES

Within this asymmetric fission model the decay constant is only the product of the assault frequency ν_0 by the barrier penetrability P. The experimental fission half-lives and theoretical predictions for the supposed most probable exit channels have been compared (see Table 2). There is a correct agreement with the experimental data on 20 orders of magnitude.

VI. SUPERHEAVY ELEMENTS

The synthesis of very heavy elements has apparently strongly progressed recently [12] but the analysis of the experimental data is discussed [13]. The macroscopic fusion barriers given by the GLDM [14, 15] standing in front of some theoretical combinations leading to ^{270}110 and ^{302}120 compound systems are displayed in Fig. 6. For the highest asymmetries the external fusion barrier energy is higher than the spherical system energy but a potential pocket appears after crossing the barrier. The nuclear system can reach a quasi-spherical shape with little excitation energy via a tunneling process but the competition with quasi-fission events in the second well is very high. This does not prove the stability of the formed system. With decreasing asymmetry the outer well progressively disappears as the outer peak. It seems that it will be very difficult to reach the eventual ground state of the superheavy elements via these almost symmetric reactions.

TABLE II: Comparison between experimental [2] and theoretical spontaneous fission half-lives of actinide nuclei.

Reaction	$T_{1/2,exp(s)}$	$T_{1/2,theo(s)}$
$^{232}_{92}U \rightarrow {}^{134}_{52}Te + {}^{98}_{40}Zr$	2.5×10^{21}	3.6×10^{16}
$^{234}_{92}U \rightarrow {}^{131}_{50}Sn + {}^{103}_{42}Mo$	4.7×10^{23}	8×10^{19}
$^{235}_{92}U \rightarrow {}^{131}_{50}Sn + {}^{104}_{42}Mo$	3.1×10^{26}	7.7×10^{23}
$^{236}_{92}U \rightarrow {}^{132}_{50}Sn + {}^{104}_{42}Mo$	7.8×10^{23}	1.0×10^{22}
$^{238}_{92}U \rightarrow {}^{132}_{50}Sn + {}^{106}_{42}Mo$	2.6×10^{23}	5.3×10^{22}
$^{238}_{94}Pu \rightarrow {}^{130}_{50}Sn + {}^{108}_{44}Ru$	1.5×10^{18}	2.6×10^{19}
$^{239}_{94}Pu \rightarrow {}^{130}_{50}Sn + {}^{109}_{44}Ru$	2.5×10^{23}	4.8×10^{22}
$^{240}_{94}Pu \rightarrow {}^{130}_{50}Sn + {}^{110}_{44}Ru$	3.7×10^{18}	4.8×10^{19}
$^{243}_{95}Am \rightarrow {}^{133}_{51}Sb + {}^{110}_{44}Ru$	6.3×10^{21}	1.1×10^{23}
$^{243}_{96}Cm \rightarrow {}^{130}_{50}Sn + {}^{113}_{46}Pd$	1.7×10^{19}	3×10^{21}
$^{243}_{96}Cm \rightarrow {}^{122}_{48}Cd + {}^{121}_{48}Cd$	1.7×10^{19}	1.6×10^{18}
$^{245}_{96}Cm \rightarrow {}^{130}_{50}Sn + {}^{115}_{46}Pd$	4.4×10^{19}	3×10^{20}
$^{248}_{96}Cm \rightarrow {}^{130}_{50}Sn + {}^{118}_{46}Pd$	1.3×10^{14}	7.7×10^{15}
$^{250}_{98}Cf \rightarrow {}^{125}_{49}In + {}^{125}_{49}In$	5.2×10^{11}	1.9×10^{9}
$^{250}_{98}Cf \rightarrow {}^{132}_{52}Te + {}^{118}_{46}Pd$	5.2×10^{11}	1.2×10^{10}
$^{250}_{98}Cf \rightarrow {}^{140}_{55}Cs + {}^{110}_{43}Tc$	5.2×10^{11}	4.9×10^{11}
$^{255}_{99}Es \rightarrow {}^{128}_{50}Sn + {}^{127}_{49}In$	8.4×10^{10}	8×10^{9}
$^{256}_{100}Fm \rightarrow {}^{128}_{50}Sn + {}^{128}_{50}Sn$	1.0×10^{4}	45
$^{256}_{100}Fm \rightarrow {}^{121}_{47}Ag + {}^{135}_{53}I$	1.0×10^{4}	82
$^{256}_{102}No \rightarrow {}^{128}_{51}Sb + {}^{128}_{51}Sb$	110	0.9×10^{-2}
$^{256}_{102}No \rightarrow {}^{116}_{46}Pd + {}^{140}_{56}Ba$	110	0.3×10^{-1}

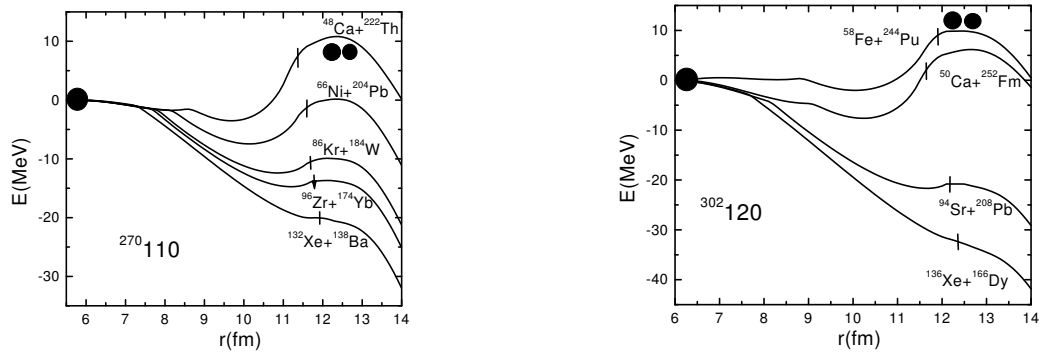

FIG. 6: Macroscopic fusion barriers for different reactions leading to the ^{270}110 and ^{302}120 nuclei. The vertical bar gives the position of the contact point.

The differences between cold fusion reactions using Pb or Bi targets and warm fusion reactions using Ca or Ti projectiles are displayed on Fig. 7 for two reactions leading to $Z = 118$ nuclei. Whatever the microscopic correction assumptions are, double-humped barriers appear in cold reactions but the excitation energy may be low. For warm reactions, the barrier against reseparation is wide and high due to the higher asymmetry and consequently to a lower Coulomb repulsion and proximity energy. There is no double-humped barriers but the excitation energy

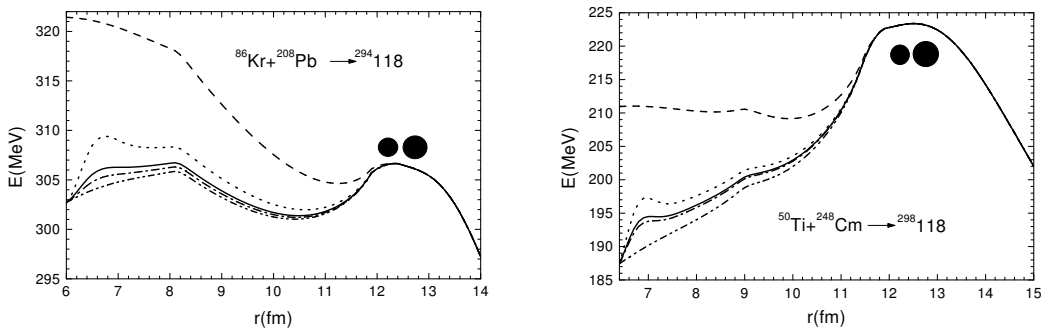

FIG. 7: Potential barriers for the ^{86}Kr +^{208}Pb and ^{50}Ti + ^{248}Cm reactions. The dashed curve gives the macroscopic barrier. The barriers corresponding to the dashed and double dotted lines incorporates a linear correction from the contact point till the sphere to reproduce the experimental Q value. The full line, dotted curve and dashed and dotted curve include the shell effects assuming respectively a proton magic number of 114, 120 and 126 and an adjustment to reproduce the Q value.

TABLE III: Comparison between experimental α decay half-lives [12] and results obtained with the GLDM [16], the DDM3Y effective interaction [17] and the VSS formulae [18].

Parent	Nuclei	Expt.	Expt.	DDM3Y	GLDM	VSS
Z	A	Q(MeV)	$T_{1/2}$	$T_{1/2}$	$T_{1/2}$	$T_{1/2}$
118	294	11.81 ± 0.06	$1.8^{+75}_{-1.3}$ ms	$0.66^{+0.23}_{-0.18}$ ms	$0.15^{+0.05}_{-0.04}$ ms	$0.64^{+0.24}_{-0.18}$ ms
116	293	10.67 ± 0.06	53^{+62}_{-19} ms	206^{+90}_{-61} ms	$22.81^{+10.22}_{-7.06}$ ms	1258^{+557}_{-384} ms
116	292	10.80 ± 0.07	18^{+16}_{-6} ms	39^{+20}_{-13} ms	$10.45^{+5.65}_{-3.45}$ ms	49^{+26}_{-16} ms
116	291	10.89 ± 0.07	$6.3^{+11.6}_{-2.5}$ ms	$60.4^{+30.2}_{-20.1}$ ms	$6.35^{+3.15}_{-2.08}$ ms	$336.4^{+173.1}_{-113.4}$ ms
116	290	11.00 ± 0.08	15^{+26}_{-6} ms	$13.4^{+7.7}_{-5.2}$ ms	$3.47^{+1.99}_{-1.26}$ ms	$15.2^{+9.0}_{-5.6}$ ms
114	289	9.96 ± 0.06	$2.7^{+1.4}_{-0.7}$ s	$3.8^{+1.8}_{-1.2}$ s	$0.52^{+0.25}_{-0.17}$ s	$26.7^{+13.1}_{-8.7}$ s
114	288	10.09 ± 0.07	$0.8^{+0.32}_{-0.18}$ s	$0.67^{+0.37}_{-0.27}$ s	$0.22^{+0.12}_{-0.08}$ s	$0.98^{+0.56}_{-0.40}$ s
114	287	10.16 ± 0.06	$0.51^{+0.18}_{-0.10}$ s	$1.13^{+0.52}_{-0.40}$ s	$0.16^{+0.08}_{-0.05}$ s	$7.24^{+3.43}_{-2.61}$ s
114	286	10.35 ± 0.06	$0.16^{+0.07}_{-0.03}$ s	$0.14^{+0.06}_{-0.04}$ s	$0.05^{+0.02}_{-0.02}$ s	$0.19^{+0.08}_{-0.06}$ s
112	285	9.29 ± 0.06	34^{+17}_{-9} s	75^{+41}_{-26} s	$13.22^{+7.25}_{-4.64}$ s	592^{+323}_{-207} s
112	283	9.67 ± 0.06	$4.0^{+1.3}_{-0.7}$ s	$5.9^{+2.9}_{-2.0}$ s	$0.95^{+0.48}_{-0.32}$ s	$41.3^{+20.9}_{-13.8}$ s
110	279	9.84 ± 0.06	$0.18^{+0.05}_{-0.03}$ s	$0.40^{+0.18}_{-0.13}$ s	$0.08^{+0.04}_{-0.02}$ s	$2.92^{+1.4}_{-0.94}$ s
108	275	9.44 ± 0.07	$0.15^{+0.27}_{-0.06}$ s	$1.09^{+0.73}_{-0.40}$ s	$0.27^{+0.16}_{-0.10}$ s	$8.98^{+5.49}_{-3.38}$ s
106	271	8.65 ± 0.08	$2.4^{+4.3}_{-1.0}$ min	$1.0^{+0.8}_{-0.5}$ min	$0.33^{+0.28}_{-0.16}$ min	$8.6^{+7.3}_{-3.9}$ min

is more than 30 MeV allowing the emission of several neutrons or an α particle.

In the table 3 the experimental α decay half-lives [12] and the predictions within the GLDM [5, 16], the Density-Dependent M3Y effective interaction [17] and the Viola-Seaborg-Sobiczewski formulae [18] are compared. The experimental Q_α values have been taken into account for the calculations. The values obtained by the GLDM and DDM3Y approaches are in agreement with the experimental data, which simply indicates that standard models describing the α decay are sufficient even for the superheavy nuclei.

VII. SUMMARY AND CONCLUSION

Exit channels of actinides and entrance channels of superheavy nuclei via the quasi-molecular shape path have been investigated within a generalized liquid drop model including the nuclear proximity energy and the microscopic corrections.

For actinides, super and hyperdeformed minima lodging isomeric states appear. The second peak corresponds to the transition from one-body shapes to two touching ellipsoids. The third barrier appears only in the asymmetric decay path and for some specific nuclei. Then, the heaviest fragment is almost a magic nucleus and it preserves its quasi-spherical shape. The other fragment evolves from an oblate ellipsoid to a prolate one and the third peak corresponds to the maximum of the shell effects in the non magic fragment and, consequently, to two touching different spheres. The barrier heights agree with the experimental results for the double and triple-humped fission barriers. The predicted half-lives follow the experimental data trend.

For superheavy elements, cold fusion reactions using Pb or Bi targets lead to double-humped fusion barriers. The two peaks are separated by a large and deep well which allows the exchange of matter between the two incoming nuclei since the neck is formed. Many quasi-fission events are highly probable. Warm fusion reactions using Ca or Ti projectiles lead to one-humped barriers but to high excitation energy. The path through more symmetric reactions does not allow to increase the probability to form these superheavy nuclei. The half-lives can be correctly reproduced using the experimental Q_α value.

[1] A. Krasznahorkay *et al.*, Phys. Lett. B **461** (1999) 15.
[2] C. Wagemans, *The nuclear fission process* (CRC Press, Boca Raton, 1991).
[3] M.G. Itkis, Yu.Ts. Oganessian, and V.I.Zagrebaev, Phys. Rev. C **65** (2002) 044602.
[4] G. Royer and K. Zbiri, Nucl. Phys. A **697** (2002) 630.
[5] G. Royer, J. Phys. G: Nucl. Part. Phys. **26** (2000) 1149.
[6] G. Royer and R. Moustabchir, Nucl. Phys. A **683** (2001) 182.
[7] G. Royer, C. Bonilla, and R. A. Gherghescu, Phys. Rev. C **67** (2003) 34315.
[8] C. Bonilla and G. Royer, Heavy Ion Physics - Acta Phys. Hung. A **25/1** (2006) 11.
[9] G. Royer and C. Gautier, Phys. Rev. C (2006) in the press.
[10] G. Royer and C. Piller, J. Phys. G: Nucl. Part. Phys. **18** (1992) 1805.
[11] W.D. Myers, *The droplet model of atomic nuclei* (Plenum, New-York, 1977).
[12] Yu.Ts. Oganessian *et al.*, Phys. Rev. C **70** (2004) 064609; Phys. Rev. C **71** (2005) 029902(E).
[13] K.E. Gregorich *et al.*, Phys. Rev. C **72** (2005) 014605 .
[14] G. Royer and R.A. Gherghescu, Nucl. Phys. A **699** (2002) 479.
[15] G. Royer, K. Zbiri, and C. Bonilla, Nucl. Phys. A **730** (2004) 355.
[16] H.F. Zhang, W. Zuo, J.Q. Li, and G. Royer, Phys. Rev. C (2006) in the press.
[17] P. Roy Chowdhury, C. Samanta, and D. N. Basu, Phys. Rev. C **73** (2006) 014612.
[18] A. Sobiczewski, Z. Patyk, and S. Cwiok, Phys. Lett. B **224** (1989) 1.